PHILOSOPHICAL MAGAZINE
2020, VOL. 100, NO. 7, 894–916
https://doi.org/10.1080/14786435.2019.1704591

Taylor & Francis
Taylor & Francis Group

Ab-initio study of the $RbEuFe_4As_4$ superconductor

Farshad Nejadsattari[a], Mohammed A. Albedah[a,b] and Zbigniew M. Stadnik[a]

[a]Department of Physics, University of Ottawa, Ottawa, ON, Canada; [b]Department of Physics, Majmaah University, Zulfi, Saudi Arabia

ABSTRACT

The results of *ab-initio* calculations of the electronic structure and magnetism of the new superconductor $RbEuFe_4As_4$ are reported. The electronic band structure and the density of states are presented and discussed in detail. The electric charge density distributions along different crystallographic planes are presented, and the origin of the chemical bonding between the constituent atoms is discussed in detail. The evidence is provided for the existence of a mixture of ionic, covalent, and metallic bonding. It is demonstrated that the magnetic moment is mainly due to the strongly localised Eu 4*f* states. An almost negligible magnetic moment carried by the Fe atoms is shown to be due to the symmetry of the Fe spin-up and spin-down states. It is demonstrated that the electrical and chemical properties of $RbEuFe_4As_4$ are closely linked with the presence of the Fe 3*d* states in the Fermi energy region. The Fermi surfaces show the presence of hole-like and electron-like pockets, respectively, at the center and corners of the Brillouin zone. The results of the calculations of the elastic properties and the ^{57}Fe and ^{151}Eu hyperfine-interaction parameters are also presented.

ARTICLE HISTORY
Received 20 June 2019
Accepted 5 December 2019

KEYWORDS
Density of states; energy band structure; magnetic moment; hyperfine interactions

1. Introduction

The discovery of a new Fe-based class of superconductors $AeAFe_4As_4$ (Ae = Ca, Sr, Eu and A = K, Rb, Cs) with the critical temperature T_c in the range 31.6–36.8 K [1–5] is significant for two reasons. First, in contrast to the intensively studied solid solutions of $(Ba_{1-x}K_x)Fe_2As_2$ or $(Sr_{1-x}Na_x)Fe_2As_2$, the Ae and A atoms in $AeAFe_4As_4$ are located at the crystallographically inequivalent positions, which causes the change of the space group from $I4/mmm$ characteristic for solid-solution superconductors to $P4/mmm$. In these new superconductors, the Ae and A layers are alternately stacked along the crystallographic c-axis between the Fe_2As_2 slabs. Consequently, the absence of structural disorder in $AeAFe_4As_4$ allows for the investigations of their intrinsic physical properties

CONTACT Zbigniew M. Stadnik stadnik@uottawa.ca Department of Physics, University of Ottawa, Ottawa, ON, Canada K1N 6N5

This article has been republished with minor changes. These changes do not impact the academic content of the article.

that are not hindered by the structural disorder present in solid-solution superconductors. Second, the presence of the Eu and Fe atoms, which potentially can order magnetically, points toward the possibility of the coexistence of two, generally incompatible phenomena, magnetism and superconductivity [6,7].

The magnetic susceptibility measurements [2,3,8–10] indicate that the $RbEuFe_4As_4$ superconductor with $T_c = 35-36$ K has a magnetic transition at ~15.0 K. Such a magnetic transition has also been found in the heat capacity data at ~15 K [9,10] and at 16.54(8) K in the ^{151}Eu Mössbauer data [11]. The isothermal magnetisation data made it possible to identify this transition as being ferromagnetic [3,10]. Ferromagnetism in $RbEuFe_4As_4$ has been hypothesised [3,10] to be associated only with the Eu magnetic moments, that is, it has been assumed that the Fe atoms have no magnetic moment. These suggestions have been confirmed experimentally in the ^{151}Eu and ^{57}Fe Mössbauer study of $RbEuFe_4As_4$ [11].

The main goal of this work is to elucidate the origin of some of the physical properties of $RbEuFe_4As_4$ via detailed electronic structure calculations. In particular, the formation and type of chemical bonds in this compound and the charge transport properties are studied. The type of chemical interactions between different atoms in $RbEuFe_4As_4$ are similar to those observed in [12]. A thorough discussion of the Fermi surface topology allows for the understanding of the electronic characteristics of $RbEuFe_4As_4$. Furthermore, a framework to test and, to some extent, predict the properties of this compound is provided. A comparison is made between the calculated physical quantities and those obtained from the magnetic and Mössbauer spectroscopy measurements.

2. Theoretical method

We performed *ab initio* calculations of the electronic structure and Mössbauer hyperfine-interaction parameters of $RbEuFe_4As_4$ in the context of density functional theory using the full-potential linearised augmented-plane-wave plus local orbitals (FP-LAPW+lo) method that is realised in the WIEN2k package [13]. This method is described thoroughly in [14]. Here, the valence wave functions in the interstitial region are expanded in spherical harmonics up to $l = 4$, while in the muffin-tin region they are expanded to a maximum of $l = 10$ harmonics. The values of 2.50, 2.50, 2.30, and 2.19 a.u. were used as the muffin-tin radii for Rb, Eu, Fe, and As, respectively. For the exchange-correlation potential, the generalised gradient approximation (GGA) scheme of Perdew, Burke, and Ernzerhof [15] was used. In addition, effective Hubbard-like interaction energies of 0.52 and 0.15 Ry were used for the Eu 4*f* and Fe 3*d* states, respectively [12,16–18]. A total number of 680 inequivalent *k*-points was used within a $32 \times 32 \times 9$ *k*-mesh in the irreducible wedge of the first Brillouin zone. A separation energy of 6.0 Ry between the valence and core states of individual atoms in a unit cell was chosen. The plane-wave cut-off parameter was set to

$R_{MT} \times K_{MAX} = 7.0$, where R_{MT} is the smallest muffin-tin radius in the unit cell and K_{MAX} is the maximum K vector used in the plane-wave expansion in the interstitial region. A convergence criterion for self-consistent field calculations was chosen in such a way that the difference in energy between two successive iterations did not exceed 10^{-4} Ry. The experimental lattice parameters (a and c) and the atomic position parameters from [11] were employed in the calculations.

3. Results and discussion

3.1. The crystal structure

Figure 1 shows the layered crystal structure of $RbEuFe_4As_4$. Various connecting rods represent the interactions between the Rb, Fe, and As atoms. One can notice that the layers of Eu atoms are entirely isolated from the Fe_4As_4 blocks and that the sheets of Rb atoms along the c-direction separate the neighbouring Fe_4As_4 blocks [11].

The type of interactions between different atoms in the $RbEuFe_4As_4$ superconductor depend on their interatomic distances. In a solid, the prevalent physical interaction between the atoms is electromagnetic in origin. Thus, the strength of the Coulomb interaction between the atoms of the compound studied is expected to determine the kind of chemical bonding between them. It is evident (Figure 1) that the density of atoms within the Fe_4As_4 blocks is higher than that within the Rb and Eu sheets. Therefore, stronger electric interactions are expected within these blocks than within the sheets. These different interactions are depicted qualitatively in Figure 1 by a dense grid of connecting rods between the Fe and As atoms in the Fe_4As_4 blocks and the lack of such connecting rods between the Eu atoms in the Eu sheets [11].

One can notice (Figure 1) that the $RbFe_4As_4$ units are separated from each other by sheets of Eu atoms. Consequently, these units are not interacting chemically with each other, as indicated by the lack of connecting rods

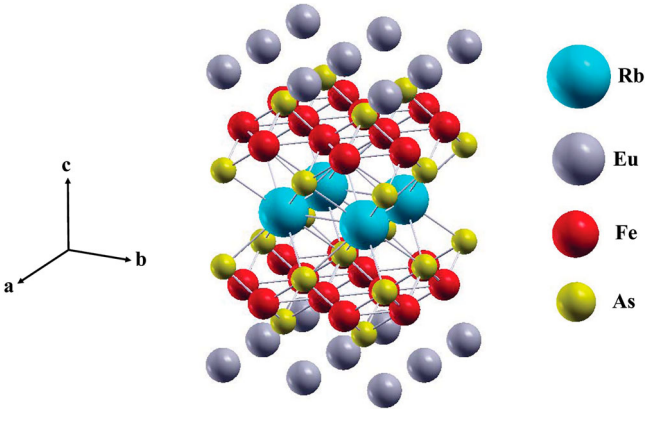

Figure 1. The layered crystal structure of $RbEuFe_4As_4$.

between the Eu atoms and the $RbFe_4As_4$ units. The Eu sheets constitute then the insulating layers along the *c*-axis. This may result from ionic interactions between the Eu sheets and the Fe_4As_4 blocks. Besides, as the tetragonal unit cell is elongated along the *c*-axis, there cannot be any significant interaction between the Eu layers. Consequently, no magnetic coupling should happen between the Eu atoms along the *c*-direction. One can thus expect that the interatomic interactions between the Eu atoms are in the *ab* plane, that is, there should exist a 2D magnetic interaction mechanism between neighbouring Eu atoms in each layer. One also notices that the Eu atoms in each layer do not interact with each other because they are isolated from one another. This is illustrated (Figure 1) by the lack of connecting rods between them [11].

The layered structure and the network of the connecting rods (Figure 1) point towards the existence of a combination of covalent and ionic bonds (*vide infra*) in the compound studied [11].

3.2. Valence charge density distributions

The valence charge density distributions along various planes are shown in Figure 2. The electronic charges of the atoms in $RbEuFe_4As_4$ were obtained through the Bader's analysis scheme [19]. The presence of a combination of ionic, covalent, and metallic bonds between different atoms in $RbEuFe_4As_4$ becomes evident by inspecting Figure 2 in detail.

As one can notice from the charge density distribution in the (001) plane [Figure 2(a)], valence charge is absent in the regions between the Eu atoms (red regions). This indicates that the Eu atoms are chemically isolated from each other. Therefore, no chemical bonding is expected to exist between these atoms. This is depicted in Figure 1 by the lack of connecting rods between the Eu atoms, which supports the argument given above. One also observes [Figure 2(a)] that the valence electrons of Eu are strongly bound to the parent atom (the yellow, green, and blue rings surrounding each Eu atom). Furthermore, a fourth-fold shape of the half-filled 4*f* shell of Eu is evident [purple regions in Figure 2(a)].

The valence charge density distribution in the (002) plane is shown in Figure 2(b). This plane consists of sheets of Rb atoms which separate the neighbouring Fe_4As_4 blocks in the *c*-direction. One can see that the charge density distribution around the Rb atoms is perfectly symmetric in the form of spheres. The electronic configuration of Rb is $[Kr]5s^1$. In fact, what is shown in this figure is the closed shell structure of the Kr atom, with the 5*s* electrons of Rb completely detached from their parent atoms and transferred to the Fe_4As_4 blocks, in particular, to the As atoms. These electrons participate in the ionic bonding between the Rb sheets and the Fe_4As_4 blocks. The Rb atoms themselves are isolated from each other due to their relatively large separation (7.34 a.u.). Consequently, no metallic interaction is likely to exist between them.

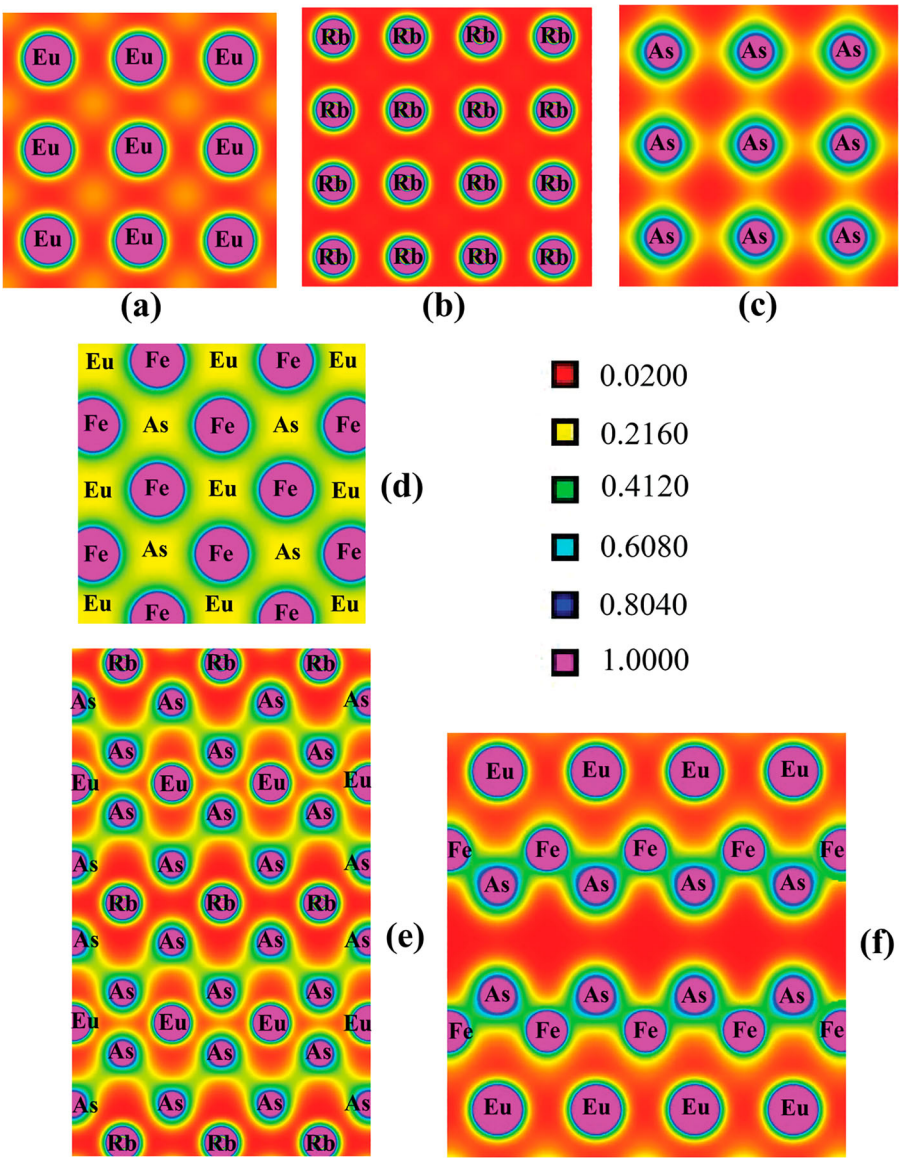

Figure 2. Electron charge density distribution (in units of e/Å^3) along the (001) (a), (002) (b), z = 0.6638 (c), z = 0.7682 (d), (110) (e), and (010) [(100)] (f) planes.

Figure 2(c) shows the valence charge density distribution in the z = 0.6638 plane which consists of the As atoms located at the 2g sites. The presence of a very weak directional covalent bonding between the adjacent As atoms can be seen (faint yellow bridges). These As atoms are isolated from each other by regions which have virtually no charge density. In contrast, the As atoms located at the 2h sites [Figure 2(d)] are involved in forming stronger covalent bonding with the neighbouring Fe atoms [the z = 0.7782 plane in Figure 2(d) passes through the Fe layers]. The valence charge density distribution in this

plane indicates that the electronic charge is spread out between the Fe–Fe and Fe–As atoms. The green regions in Figure 2(d) correspond to the charge distribution of the Fe 4*s* electrons throughout the Fe layers, which leads to the formation of the metallic Fe-Fe bonds. The electronic transport in the superconductor studied is expected to occur predominantly within these Fe layers and, to a smaller extent, within the metallic Fe_4As_4 blocks.

The valence charge density distribution in the (110) plane is shown in Figure 2(e). This plane passes through the Eu and Rb atoms, and also through the As atoms located at the 2*h* sites. The presence of the As–As covalent bonds is visible as the electrons are delocalised between these atoms (green regions). Furthermore, a complete charge transfer from the Rb and Eu atoms to the As layers is evident (red regions indicating the virtual absence of charge). This leads to the formation of two sets of ionic bonds: a strong ionic bond between the alkali Rb layers and the metalloid As layers, and a weaker ionic bond between the layers of the Eu and As atoms. One can interpret this result by considering the differences between the electronegativity of the Rb (0.82) and the Eu (1.2) atoms and that of the As (2.18) atoms. Based on these electronegativity values, the Rb–As bond is expected to be stronger than the Eu–As bond. These two sets of ionic bonding are depicted in Figure 2(e) by two red regions of different intensity. No electronic transport is expected to exist between the separate As layers due to the formation of these ionic bonds. As mentioned earlier, any transport (whether electrical or thermal) must be along the Fe_4As_4 blocks.

When one considers the symmetry of the space group *P*4/*nmm* and the crystal basis of $RbEuFe_4As_4$, then it becomes clear that the charge density distributions in the (010) and (100) planes are the same [Figure 2(f)]. These planes pass through the Eu, As at the 2*g* sites, and Fe atoms. Because of the virtual absence of charge density [red regions in Figure 2(f)], it is clear that the sheets containing the Eu atoms are isolated from each other. The delocalisation of the valence charges of the As and Fe atoms leads to the formation of strong covalent As-Fe bonds. The green regions in between the As and Fe atoms indicate the presence of a relatively high charge density.

3.3. Density of states

In this section, we bring the results of the DFT calculations for the total and partial density of states (DOS) in $RbEuFe_4As_4$ using the modified tetrahedron method [20].

The spin-resolved, total, and atom-resolved DOS in the ferromagnetic $RbEuFe_4As_4$ is shown in Figure 3. The characteristic DOS features occur in four distinct energy regions. The DOS in the first energy region, which lies below ~ -10 eV, is due to the atomic-like core electrons of Rb and As atoms. More specifically, the Rb core electrons contribute to the DOS in the energy

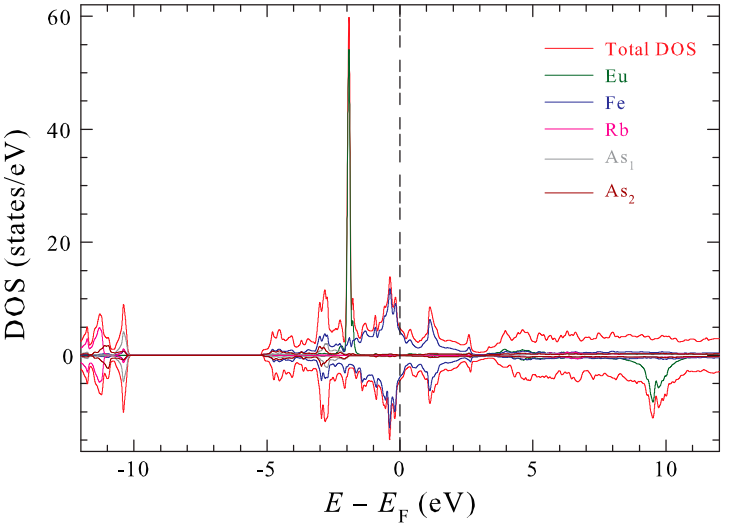

Figure 3. Spin-resolved, total and atom-resolved DOS in ferromagnetic $RbEuFe_4As_4$.

region below −11.1 eV whereas the contribution from the As core electrons is in the energy region between −11.6 and −10.1 eV. As these core states lie deep in energy, they practically do not contribute to any of the physical properties of the compound studied. The DOS of these states resembles that of isolated atomic states of the Rb and As atoms.

The second energy region between −10.1 and −5.2 eV contains a ∼5 eV energy gap. This gap separates the core states from the semi-core and valence states. Its relatively large width ensures that the core states are isolated in energy. In addition, the electrons corresponding to these states are entirely bound to their host nuclei by strong electrostatic forces.

The DOS in the third energy region (between −5.0 and 3.0 eV), which includes the Fermi energy (E_F), determines most of the physical properties of $RbEuFe_4As_4$. Here the semi-core, valence, and conduction states form a continuum of DOS. A noticeable dip in the DOS at ∼0.7 eV indicates the presence of a pseudogap that is due to a few Fe states. This pseudogap can be attributed to the Coulomb repulsion of the Fe electrons. The T_c values of the high-temperature superconductors are in the range 30–250 K [21]. For the $RbEuFe_4As_4$ superconductor, $T_c \approx 35.5$ K [2,3,8–10]. A relatively small energy gap is expected to exist in superconductors. It opens up above T_c and increases with increasing temperature. DFT calculations give the results for the ground state of a system. Therefore, one does not expect any energy gap across the E_F region in $RbEuFe_4As_4$ at temperatures below T_c. The predicted existence of a small pseudogap below T_c in the DOS of the Fe-3*d* contribution (Figure 3) constitutes a signature of the superconductivity in the compound studied. Such pseudogaps have also been observed experimentally for compounds of similar structure and containing the Fe-As blocks [22]. In addition, the Hubbard

models for high-temperature superconductors predict the coexistence of magnetic ordering and superconductivity [23].

The delocalised Fe states dominate the energy region between −1.5 eV and E_F (Figure 3). They form the valence states that are responsible for the formation of the metallic bonds between the Fe atoms within the Fe_4As_4 blocks. A sharp peak in the spin-up DOS in the energy region between −2.0 and −1.6 eV arises entirely from the localised Eu 4*f* electrons. The Eu 4*f* states have minimum overlap with the Fe states, which can indicate the insulating characteristics of the compound studied. This agrees with the reasoning presented above (section B.). Below the energy region dominated by the Eu 4*f* states (between −3.6 and −2.1 eV), one observes contributions from the As and Fe atoms. The overlap between the As and Fe states in this region is indicative of covalent bonding between the As and Fe atoms. The valence and semi-core electrons form these chemical bonds. This covalent bonding can be considered to arise from the hybridisation between the Fe 3*d* states with those of the As 4*p* states.

The fourth energy region, which extends from 3.2 eV upwards, consists of empty states as no electrons are likely to be excited into these states. A relatively large peak in the spin-down DOS between 8.2 and 10.7 eV originates from the Eu 4*f* electrons. The origin of these localised Eu 4*f* states is discussed below in terms of Coulomb-interaction arguments.

A characteristic feature of the DOS in Figure 3 is that in contrast to the energy separation and magnitude difference between the Eu spin-up and spin-down states, the spin-up and spin-down DOS contributions from the other atoms are symmetric. This results in almost negligible magnetic moments of the Rb, Fe, and As atoms (*vide infra*). As a consequence of the high asymmetry observed in the Eu DOS from its two spin components, a large magnetic moment of the Eu atoms is expected. Thus, the magnetism of $RbEuFe_4As_4$ originates mainly from the Eu atoms.

The near Fermi energy region is dominated by the Fe 3*d* states and, to a far less extent, by the As 4*p* states. These states are ultimately responsible for the conductive nature of $RbEuFe_4As_4$. On the other hand, there is almost zero DOS contribution from the Eu and Rb atoms in the Fermi energy region. This suggests that the conductivity in $RbEuFe_4As_4$ must occur along specific directions. In other words, anisotropic conductivity along the Fe-As bonds is expected.

Figure 4(a) displays the spin-resolved DOS due to the Rb atoms for the 3*d* and 4*p* orbitals. The symmetry of the spin-up and spin-down states is evident. Consequently, one expects no magnetic moment for the Rb atoms in $RbEuFe_4As_4$. One also observes that there is virtually no Rb contribution to DOS in the Fermi energy region. The core states of Rb are of the 4*p* character, and their DOS shows three peaks at −11.7, −11.3, and −10.3 eV. The 4*p* core states occupy two energy regions: one between −12.0 and −10.8 eV and the other between −10.7 and −10.2 eV.

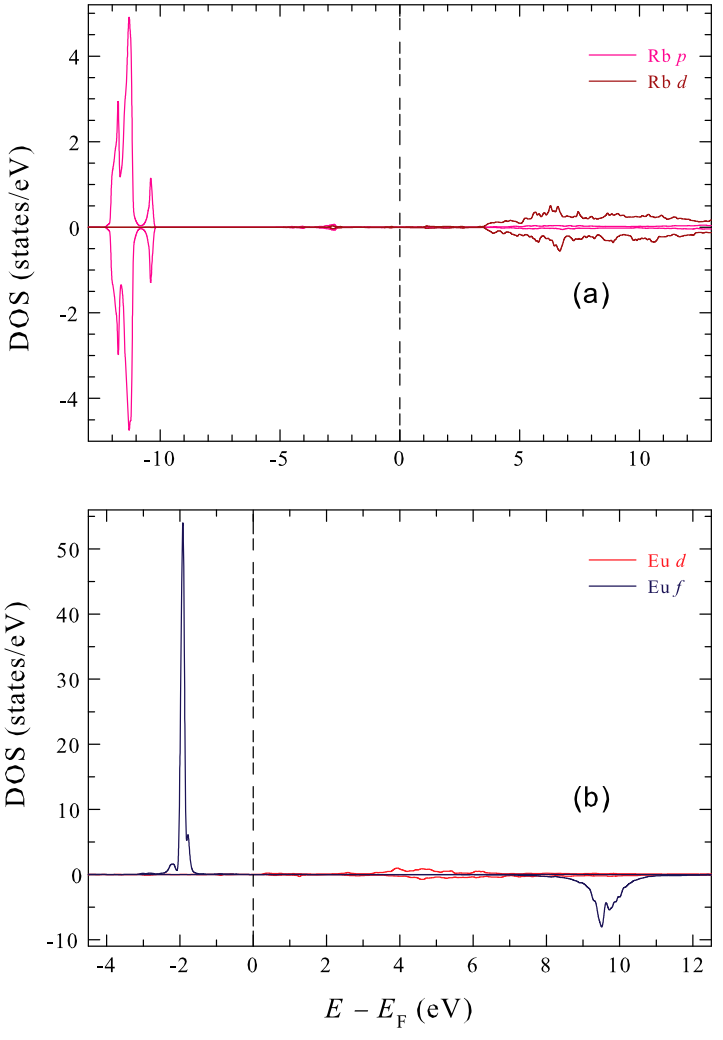

Figure 4. Spin-resolved DOS of the Rb (a) and Eu (b) atoms in ferromagnetic $RbEuFe_4As_4$.

The Rb 3*d* states are mainly distributed in the energy region above 3.5 eV [Figure 4(a)]. These conduction states are less numerous than those of the core 4*p* states and possess metallic-like characteristics. The 3*d* orbitals of Rb are essentially empty as they lie relatively high above E_F.

A highly localised DOS due to the Eu 4*f* states, as opposed to the extended and much less numerous DOS due to the Eu 3*d* states, can be seen in Figure 4(b). The contribution to DOS from the Eu 3*d* states is minimal and symmetric for both spin orientations, whereas that from the Eu 4*f* is very large and asymmetric. The majority spin contribution is from the sharp 4*f* up states of Eu that are localised between −2.4 and −1.5 eV. On the other hand, the minority 4*f* down states of Eu lie in a relatively high-energy region (between 8.4 and 10.5 eV). Under normal conditions, these states are empty as no electron can have

enough energy to occupy them. This significant difference in the population of the two spin configurations accounts for a significant magnetic moment found experimentally in $RbEuFe_4As_4$ [3]. The majority of the Eu 3*d* states also lie above E_F. Though few, they are widely spread between 3.6 and 10.8 eV.

Figure 5(a) shows the spin-resolved DOS originating from the Fe 4*s*, 3*p*, and 3*d* orbitals. It is evident that the main contribution to the DOS is from the Fe 3*d* states and that the presence of such states across E_F accounts for the conductive

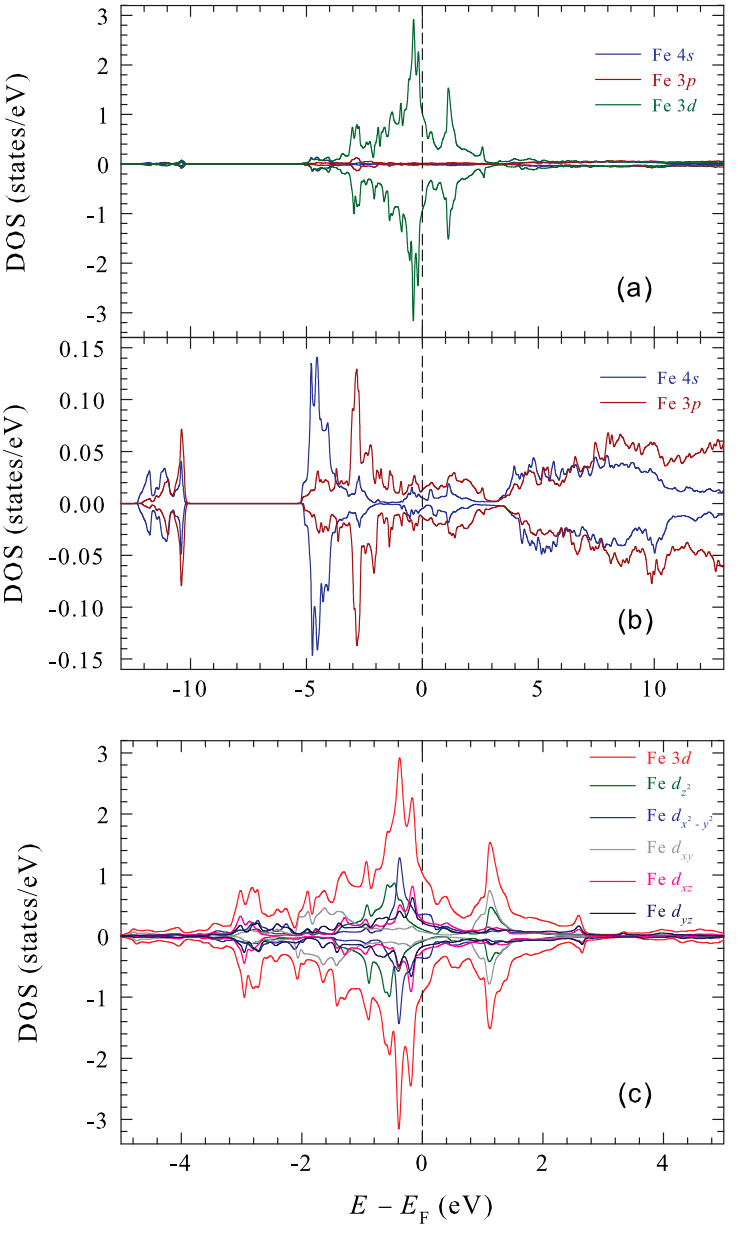

Figure 5. Spin-polarised, Fe orbital-resolved DOS [(a) and (b)] and Fe *d*-orbital-resolved DOS (c).

nature of the $RbEuFe_4As_4$ compound. The preponderance of the Fe states spans an energy region between −5.0 and 2.8 eV. The most intense peak in the Fe DOS occurs at ~ -0.4 eV, and then the Fe DOS decreases as one moves across E_F. A local minimum at 0.6 eV and a local maximum at ∼1.0 K in the Fe DOS are observed. It is clear from Figure 5(a) that the spin-up and spin-down contributions to the Fe DOS are almost perfectly symmetric. This suggests a small magnetic moment carried by the Fe atoms in $RbEuFe_4As_4$. The contribution to the Fe DOS from the 4*s* and 3*p* states is almost negligible (the latter contributes slightly in the energy region between −3.0 and −1.8 eV).

The Fe 4*s* and 3*p* contributions to the Fe DOS are shown in more detail in Figure 5(b). One observes that in the energy region above 3.2 eV, the DOS is widely spread and there is an overlap between the 4*s* and 3*p* states. This broad DOS is indicative of the existence of metallic bonds. On the other hand, below E_F, the 4*s* and 3*p* states are fairly separated with several peaks in the DOS. These are localised valence and semi-core states. The strongest spin-up 3*p* and 4*s* DOS peaks are at −2.8 and −4.5 eV, respectively. A small contribution of the Fe core states to the DOS is in the energy region between −12.3 and −10.1 eV. One notices that the Fermi energy region is almost empty of the Fe 4*s* and 3*p* states.

As mentioned earlier, the most significant contribution to the Fe DOS originates from its 3*d* orbitals. Figure 5(c) displays the individual *d*-orbital-resolved contributions to the Fe *d* DOS. The large peak in the Fe DOS originates mainly from the $d_{x^2-y^2}$ states located at about −0.4 eV. These states are mainly localised and exist below E_F. The small peak in the DOS above E_F at about 1.0 eV originates from the d_{xy} and d_{z^2} orbitals. The d_{z^2} states also extend to the region below E_F and they peak at around −0.5 eV. The majority of the d_{xz} states are located in the vicinity of E_F and contribute to the peak at −0.15 eV. The conductive nature of $RbEuFe_4As_4$ can be related to these states. The smallest contribution to the Fe 3*d* DOS is from the d_{yz} states which are non-localised and predominantly spread below E_F into the valence region.

Figure 6(a) displays the DOS due to the As_1 and As_2 atoms located at two different Wyckoff positions 2*g* and 2*f*, respectively [11]. One can notice that although the states due to the As_1 and As_2 atoms occupy the same energy region, they are slightly displaced from each other. As core states lying between −12 and −10 eV are localised and are atomic-like. The semi-core and valence states span an energy region between −5.2 and −1.6 eV and display sharp peaks in DOS between −3.0 and −2.7 eV. The conduction states extend from E_F to 2.8 eV. Above 2.8 eV, the mainly empty metallic, and perfectly overlapping As_1 and As_2 states are located. As a result of the presence of non-localised and overlapping states, the bonding between the As atoms in the compound studied is covalent.

As one can observe in Figure 6(b), the core states lying deep in energy consist consist mainly of 4*s*-type orbitals of closed-shell structure, whereas the states

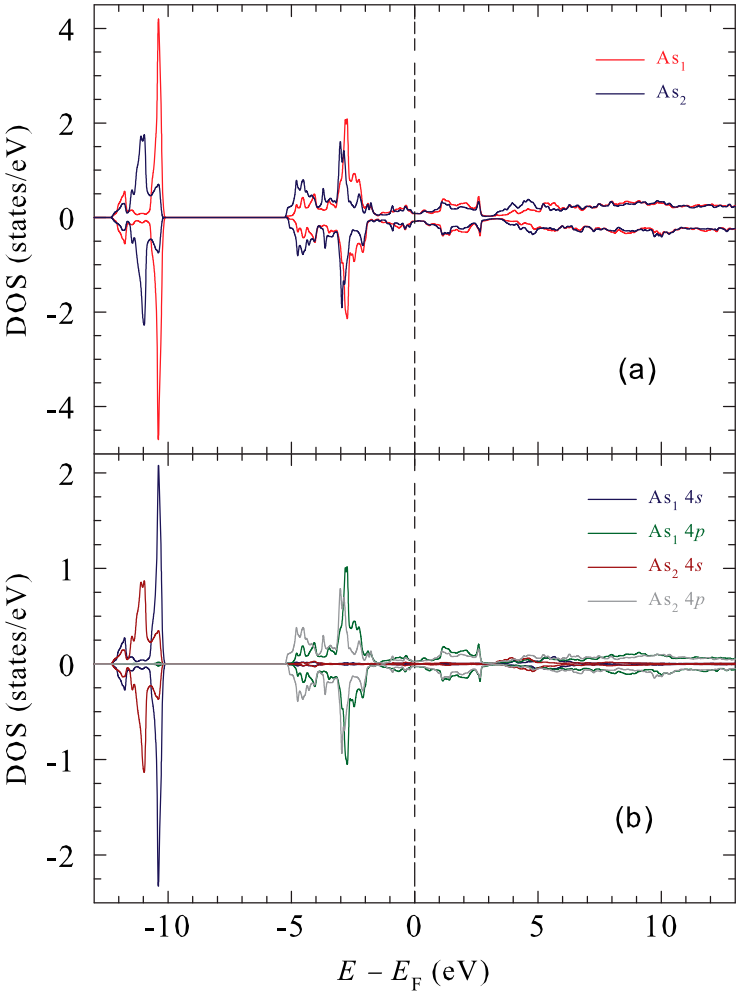

Figure 6. Spin-resolved DOS of As (a) and spin-resolved, orbital-resolved DOS of As.

closer to E_F are dominated by the relatively extended 4*p* states (between −5.2 and −1.7 eV). The As_1 4*p* states are slightly more numerous than the As_2 4*p* states. The spin-up and spin-down contributions to the DOS from both atoms are almost identical, which yields nearly zero magnetic moments of the two As atoms.

3.4. Energy band structure

The calculated band structure of the ferromagnetic $RbEuFe_4As_4$ (Figure 7) spans an energy region between −10 and 10 eV. It can be noted that for the spin-up configuration [Figure 7(a)], the energy bands above E_F are relatively dispersive, which indicates a conductive nature of the states residing along these bands. In the vicinity of E_F, the bands are less dispersive, and thus correspond to localised states originating from the Fe 3*d* orbitals. These states cross the Fermi level

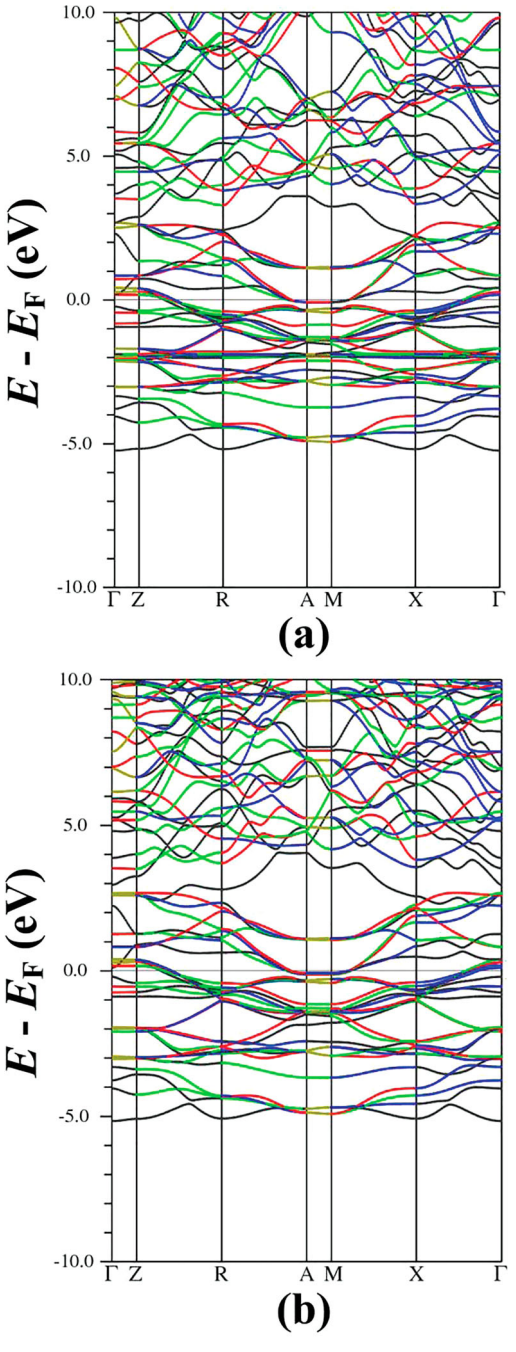

Figure 7. Spin-up (a) and spin-down band structures of ferromagnetic $RbEuFe_4As_4$.

mainly midway between the X and Γ-points, and also between the Z and R points. These Fermi energy crossing bands are responsible for the conductive nature of $RbEuFe_4As_4$. The bands at about −2 eV are very dense and flattened. They originate from the Eu 4*f* state contributions. The small

dispersion of these bands indicates that they correspond to extremely localised states. The small curvature of the bands points to a large corresponding effective mass m^* ($m^* \sim [\nabla^2_{\mathbf{k}} E(\mathbf{k})]^{-1}$), that is, the carriers occupying these bands are essentially immobile. The semi-core states of As and Rb lie further down, between −4 and −3 eV [Figure 7(a)]. They are relatively dispersive in energy, which reflects their *p* and *s* character. There are no energy bands below −5 eV [Figure 7(a) does not include energies below −10 eV where the atomic core states reside].

The characteristics of the bands for the spin-down configuration [Figure 7(b)] are mostly the same as those for the spin-up configuration. The only difference is in the Eu 4*f* states which lie high above E_F (at ∼10 eV) and are numerous and less localised. Similarly to the spin-up configuration, the Fermi region is dominated by the Fe 3*d* states.

A common feature that can be observed for both spin-up and spin-down configurations (Figure 7) is the merging of the energy bands along the high-symmetry points in the Brillouin zone, such as Γ, X, and R. As one moves away from these points, the symmetry on the *k*-space is broken and consequently the bands start to diverge from each other. The electronic states along these high-symmetry directions are localised and nested. This indicates that any carrier in these regions will be subject to a null net electrostatic force, thus confining the carriers into regions in the vicinity of these particular points.

3.4.1. Atom-resolved energy band structure

The spin-polarised energy bands originating from the Fe, Eu, Rb, As_1, and As_2 atoms are presented in Figure 8. In this figure, the thickness of the bands indicates their relative weight, that is, their relative contribution to the energy band structure of $RbEuFe_4As_4$. One can notice that the Fe energy bands [Figure 8(a, b)] dominate the Fermi energy region and extend from −4.0 to 3.0 eV. These bands are mainly composed of the Fe 3*d* orbitals. The contributions from these states become smaller as one moves away from the Fermi region in both directions and thinner bands depict this in Figure 8(a,b). Moreover, no spin polarisation in the Fe bands is observed. This confirms the result of our earlier DOS calculations and agrees with the experimentally determined [11] zero intrinsic hyperfine magnetic field at ^{57}Fe nuclei, and thus zero Fe magnetic moment.

In contrast to the spin-resolved Fe energy bands, there is a large difference between the spin-up and spin-down Eu energy bands [Figure 8(c,d)], both in energy and in weight (thickness of the bands). This will lead eventually to a large magnetic moment carried by the Eu atoms. The energy bands for a spin-up configuration [Figure 8(c)] are mainly confined to the energy region around −2.0 eV, whereas for a spin-down configuration [Figure 8(d)] the numerous Eu 4*f* bands are located above 9.0 eV. This observation is consistent with an earlier discussion of the DOS originating from the Eu 4*f* states. In both

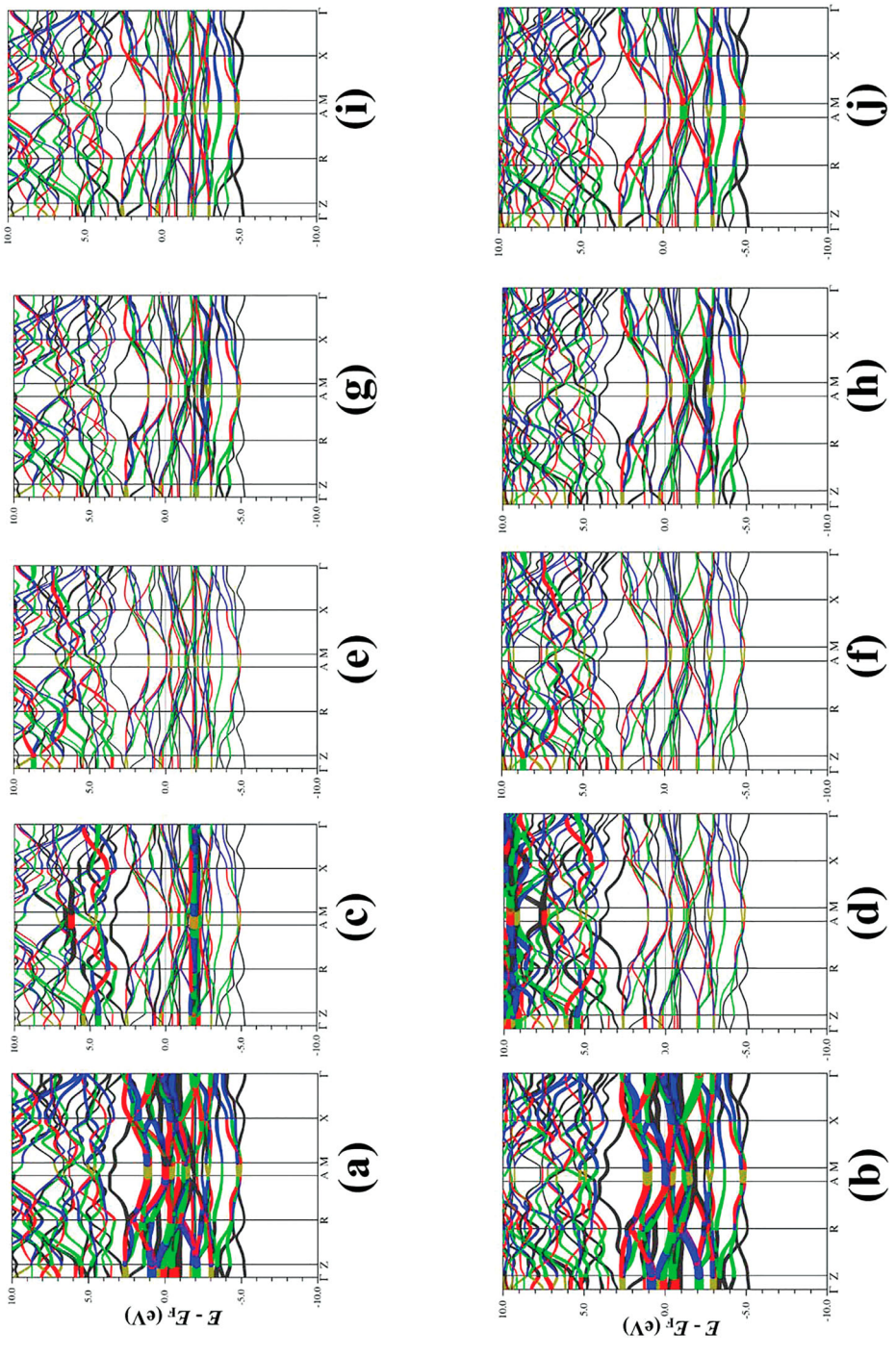

Figure 8. Spin-polarised and atom-resolved band structure of ferromagnetic $RbEuFe_4As_4$. The Fe spin-up (a) and spin-down (b) contributions. The Eu spin-up (c) and spin-down (d) contributions. The Rb spin-up (e) and spin-down (f) contributions. The As_1 spin-up (g) and spin-down (h) contributions. The As_2 spin-up (i) and spin-down (j) contributions.

figures in the energy region above 5 eV, a smaller but symmetric contribution from the Eu 3*d* states is observed.

As one can notice in Figure 8(e,f), the relatively thin bands indicate the small contribution of the Rb states to the total band structure of the superconductor. The contributions from both spin configurations are identical along all directions in the Brillouin zone, and consequently, the magnetic moment of the Rb atoms in $RbEuFe_4As_4$ is negligible. A careful examination of Figure 8(e,f) shows that there is a small contribution from the Rb energy bands across E_F (as indicated by the thinner bands).

At first glance at Figure 8(g–j) one can notice that the As_1 and As_2 atoms do not contribute significantly to the energy band structure of the compound studied. There are, however, two energy regions in which the As contribution is not negligible. The first energy region is in the neighbourhood of E_F. Here, although the bands are thin, they are depicted thicker than the rest of the bands. The other energy region is around −2.0 eV. Both energy regions contain a small number of bands originating from the As atoms.

3.4.2. Orbital-resolved energy band structure of Fe

Figure 9 shows the spin-polarised band structure resulting from various Fe 3*d*-orbitals. One observes that a few bands emerging from the Fe $d_{x^2-y^2}$ orbitals [Figure 9(a,b)] cross the E_F region. Multiple hole-like bands exist around the high symmetry points Γ, X, M, A, and R. Four regions of electron-like bands are observed midway between the connecting high symmetry directions of Γ–X, M–X, A–R, and R–Z. One also observes a negligible dispersion along the A–M and Γ–Z directions. This observation is based on the presence of a tiny slope of the bands in this energy region.

The bands originating from the d_{z^2} orbitals [Figure 9(c,d)] are similar to those due to the $d_{x^2-y^2}$ orbitals. However, they are heavier across E_F and lighter below E_F.

Most of the bands origination from the d_{xy}-orbitals are in the conduction region between 0.9 and 1.0 eV [Figure 9(e,f)]. The contribution to the band structure of $RbEuFe_4As_4$ from the d_{xy} orbitals [Figure 9(g,h)] and the d_{yz} orbitals [Figure 9(i,j)] is minimal. One can conclude that the properties of the compound studied are determined mainly by the $d_{x^2-y^2}$ and d_{z^2} orbitals.

3.4.3. Fermi surfaces

The Fermi surfaces calculated in the first Brillouin zone are displayed in Figure 10. The surfaces are plotted along the indicated high symmetry points. One observes in Figure 10(a) a four-fold hole-like Fermi surface sheet in the central region of the Brillouin zone and along the Γ–Z direction. The triplicate hole pockets at the center of the Brillouin zone are not of the same size. The four corners of the Brillouin zone consist of the Fermi surface sheets of electron-like character, i.e. the electron pockets are aligned parallel to the A–M direction.

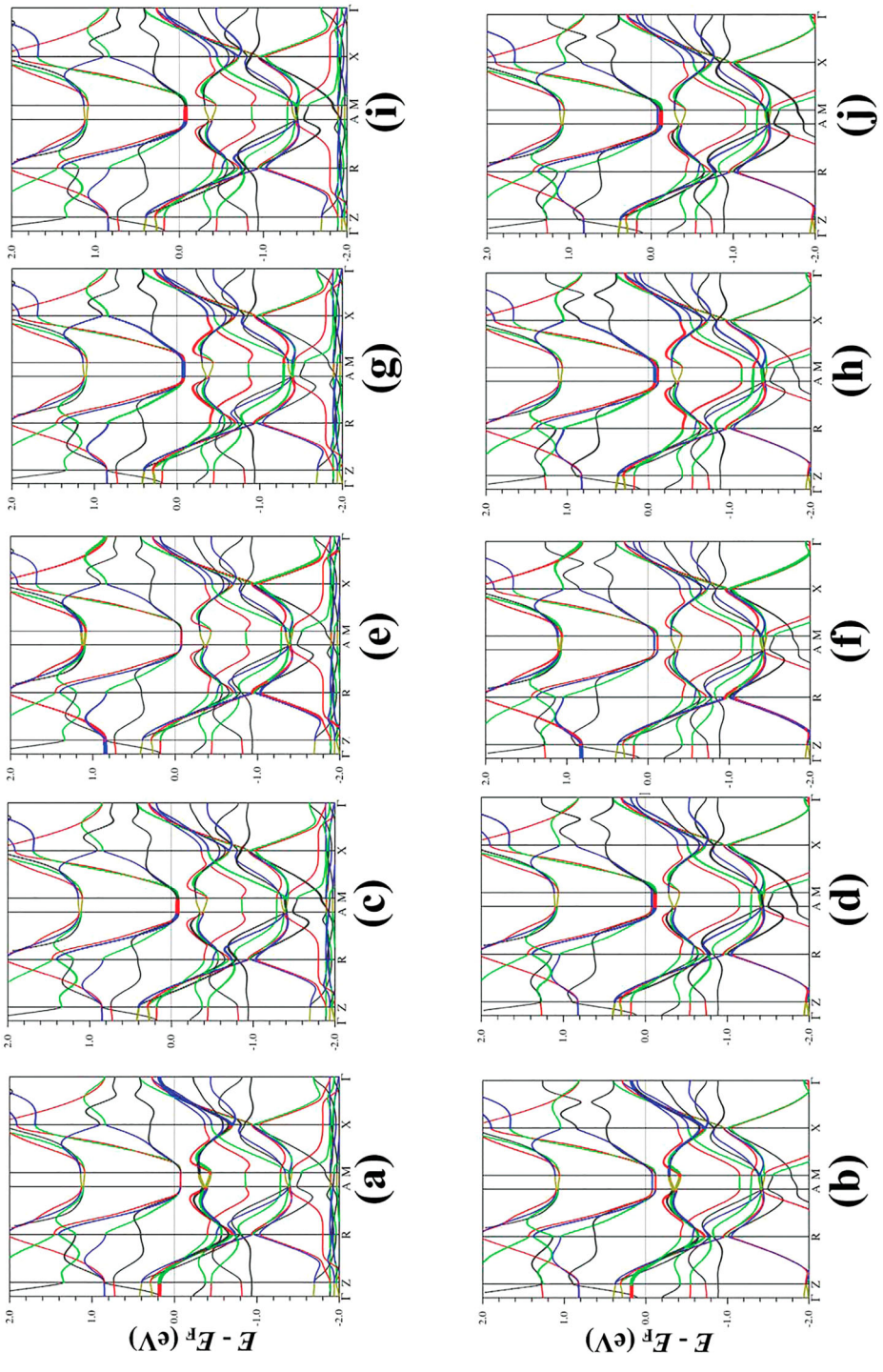

Figure 9. Spin-polarised band structure resulting from the Fe orbitals $d_{x^2-y^2}$ [(a), (b)], d_{z^2} [(c), (d)], d_{xy} [(e), (f)], d_{xz} [(g), (h)], and d_{yz} [(i), (j)].

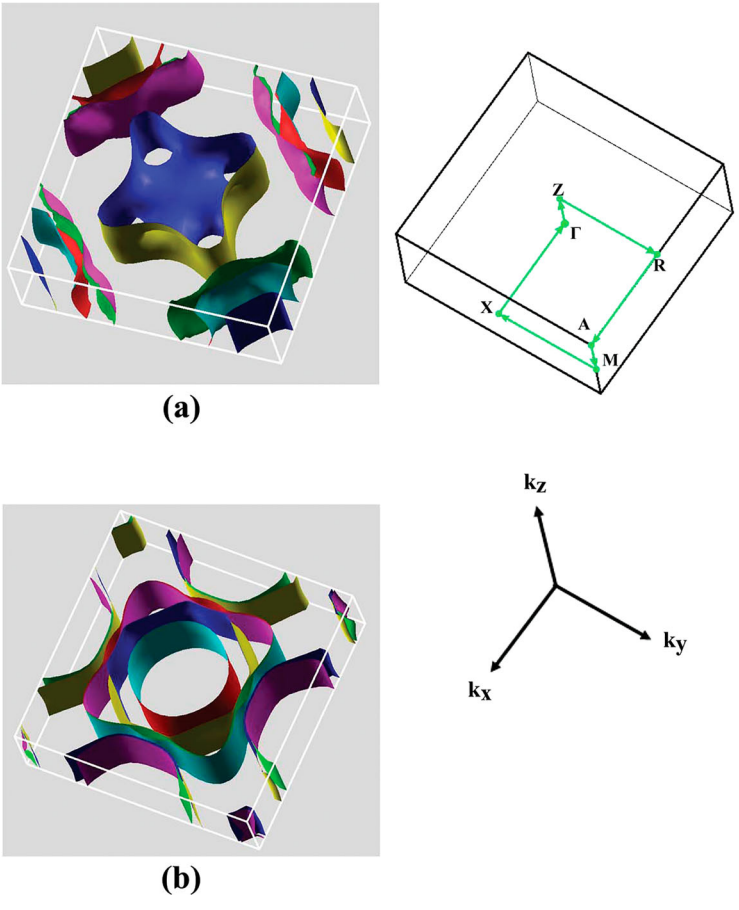

Figure 10. Fermi surfaces of the ferromagnetic $RbEuFe_4As_4$ for the spin-up (a) and spin-down (b) configurations.

For the spin-down configuration [Figure 10(b)], three hole-like Fermi sheets about the Γ point are observed. The central sheet is in the form of a uniform cylinder, and no dispersion along the k_z direction is observed. Two distorted cylindrical sheets surrounding the X point can be seen (they are not present for the spin-up configuration). The densities of the Fermi surface sheets in two spin configurations are different (Figure 10). This results from the fact that the bands in the spin-up configuration are closely packed along the Fermi level as compared to those for the spin-down configuration. For example, in Figure 10(a) one only observes a single Fermi surface at the center that is related to a hole pocket. The same Fermi surface topologies have been found in similar Fe-based superconductors [24–26].

The superconductivity of the compound studied has also a signature in the Fermi surface topology (Figure 10). The *d*-wave symmetry of the superconducting gap in high-temperature superconductors is an accepted fact that is used in the development of superconductivity theories and in the interpretation of the

experimental results [27]. The largest gaps on the Fermi surfaces (Figure 10) are at the edges of the Brillouin zone and are located in the areas around the centre of the Brillouin zone boundary surfaces. The Fe 3*d* states near the E_F level play a similar role as those in other Fe-based superconductors [28].

3.5. Elastic properties

Some of the elastic parameters of $RbEuFe_4As_4$ were calculated for the optimised lattice parameters obtained from the minimisation of the total energy (Figure 11). The energy minimum of −55927.92 Ry occurs for the optimised volume of the primitive tetragonal unit cell of 1214.6259 a.u.^{3}, which is somewhat smaller than the value of 1358.3110 a.u.^{3} derived from the Rietveld refinement [11]. The calculated equilibrium bulk modulus, B_0 is 138.9 MPa, and its pressure derivative is 25.6. These parameters were obtained using the Birch-Murhanghan equation of state [29,30].

3.6. Magnetic moments and Mössbauer hyperfine parameters

The calculated magnetic moment per formula unit of $RbEuFe_4As_4$ is 6.913 μ_B. This value consists of the contribution (6.7301 μ_B) from the muffin-tin and 0.2099 μ_B) from the interstitial regions. The calculated magnetic moments carried by the Rb, Eu, Fe, As_1, and As_2 atoms are 0.0005, 6.9072, −0.0450, 0.0031, and −0.0152 μ_B, respectively. The calculated Eu magnetic moment is slightly larger than the experimental moment of 6.5 μ_B at 2 K [3] that was derived from the magnetisation measurements. The nearly vanishing calculated magnetic moment of the Fe atoms is in excellent agreement with the experimental observation via ^{57}Fe Mössbauer spectroscopy [11] of zero intrinsic magnetic moment of the Fe atoms down to 2.1 K. The values of the calculated magnetic moments indicate that ferromagnetism in $RbEuFe_4As_4$ is associated exclusively with the Eu atoms.

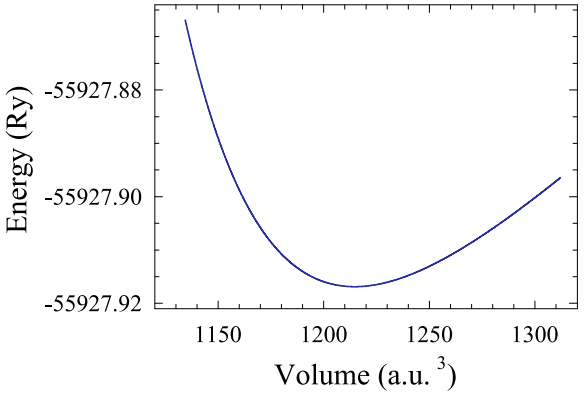

Figure 11. Total energy as a function of primitive cell volume of $RbEuFe_4As_4$.

Three types of hyperfine-interaction parameters can be derived from the fits of Mössbauer spectra [31,32]. These are: the isomer shift δ_0, the principal component of the electric field gradient tensor V_{zz} and the asymmetry parameter η, and the hyperfine magnetic field H_{hf}. They can also be obtained from *ab initio* calculations carried out for any crystalline compound with known crystal structure [33].

The isomer shift can be calculated from the expression $\delta_0 = \alpha[\rho(0) - \rho_{\text{ref}}(0)]$, where $\rho(0)$ and $\rho_{\text{ref}}(0)$ are, respectively, the total electron densities at the Mössbauer nucleus in the compound studied and in the reference material, and α is a calibration constant. In calculating $\rho(0)$, relativistic spin-orbit effects were included to account for the possibility of the penetration of the $p_{1/2}$ electrons into the ^{57}Fe nuclei [34]. The reference material for ^{57}Fe Mössbauer spectroscopy is α-Fe metal (with the *bcc* structure and the lattice constant of 2.8665 Å). The calculated $\rho(0)$ and $\rho_{\text{ref}}(0)$ are 15308.530 and 15309.918 $(\text{a.u.})^{-3}$, respectively. Using the calibration constant $\alpha = -0.291\ (\text{a.u.})^3(\text{mm/s})$ [35], the calculated values of $\rho(0)$ and $\rho_{\text{ref}}(0)$ imply that $\delta_0 = 0.404$ mm/s (analogous calculations of δ_0 for ^{151}Eu Mössbauer spectra cannot be done as the corresponding α has not been established yet). The calculated δ_0 is close to the experimental value of 0.494(2) mm/s [11].

The measured H_{hf} consists of three main contributions [36]: the Fermi contact term H_c, the magnetic dipolar term, H_{dip}, and the orbital moment term, H_{orb} [31,32]. The first term is generally much greater in magnitude than the other two terms. The Fermi contact term is calculated from the expression $H_c = \frac{8\pi}{3}\mu_B^2(\rho_\uparrow(0) - \rho_\downarrow(0))$, where $\rho_\uparrow(0)$ and $\rho_\downarrow(0)$ are the spin-up and spin-down densities at the Mössbauer nucleus, respectively. The calculated magnitudes of H_c at the ^{57}Fe and ^{151}Eu nuclei are 8.9 and 266.5 kOe, respectively. These should be compared with the corresponding experimental H_{hf} values (at 0 K) of 6.17(2) and 257.4(4.3) kOe [11].

The calculated V_{zz} and η are 5.270×10^{20} V/m^2 and 0.8734 for ^{57}Fe Mössbauer spectra [11]. The calculated V_{zz} and η imply that the value of the quadrupole splitting $\Delta = \frac{1}{2}\, eQ|V_{zz}|\sqrt{1 + \eta^2/3}$ (Q = 0.15 b is the electric quadrupole moment of the 14.4-keV excited state of ^{57}Fe nucleus [37]) should be 0.0921 mm/s. For ^{151}Eu Mössbauer spectra, the calculated V_{zz} and η are -49.659×10^{20} V/m^2 and 0.0 (the zero value is consistent with the point symmetry 4/*mmm* of the Eu site). The experimental Δ (at 0 K) of 0.1182 mm/s [11] is in excellent agreement with the predicted value of 0.0921 mm/s. Similarly, good agreement is found between the calculated values of V_{zz} and η and the corresponding experimental values (at 0 K) of $-47.0(6) \times 10^{20}$ V/m^2 and 0.0 derived from the ^{151}Eu Mössbauer spectra [11].

4. Conclusions

We present the results of *ab-initio* calculations of the electronic structure, magnetism, and hyperfine interaction parameters of the new $RbEuFe_4As_4$

superconductor. The calculations suggest the presence of a mixture of ionic, covalent, and metallic bonding between the constituent atoms. We discuss in detail the electronic band structure and the density of states. We show that, in agreement with the experimental results, the magnetic moment is due to the strongly localised Eu 4*f* states. We demonstrate that an almost zero magnetic moment carried by the Fe atoms results from an apparent symmetry of the spin-up and spin-down states. The Fermi surfaces along various directions in the Brillouin zone are presented. We show that the calculated ^{57}Fe and ^{151}Eu Mössbauer hyperfine interaction parameters are in good agreement with the corresponding parameters derived from the Mössbauer spectra.

Disclosure statement

No potential conflict of interest was reported by the authors.

Funding

This work was supported by the Natural Sciences and Engineering Research Council of Canada (NSERC).

References

[1] A. Iyo, K. Kawashima, T. Kinjo, T. Nishio, S. Ishida, H. Fujihisa, Y. Gotoh, K. Kihou, H. Eisaki, and Y. Yoshida, *New-structure-type Fe-based superconductors: $CaAFe_4As_4$ (A = K, Rb, Cs) and $SrAFe_4As_4$ (A = Rb, Cs)*, J. Am. Chem. Soc. 138 (2016), pp. 3410–3415

[2] K. Kawashima, T. Kinjo, T. Nishio, S. Ishida, H. Fujihisa, Y. Gotoh, K. Kihou, H. Eisaki, Y. Yoshida, and A. Iyo, *Superconductivity in Fe-Based Compound $CaAFe_4As_4$ (A = Rb and Cs)*, J. Phys. Soc. Jpn. 85 (2016), p. 064710.

[3] Y. Liu, Y.-B. Liu, H. Jiang, Z.-C. Wang, A. Ablimit, W.-H. Jiao, Q. Tao, C.-M. Feng, Z.-A. Xu, and G.-H. Cao, *Superconductivity and ferromagnetism in hole-doped $RbEuFe_4As_4$*, Phys. Rev. B 93 (2016), p. 214503.

[4] Y. Liu, Y.-B. Liu, Q. Chen, Z.-T. Tang, W.-H. Jiao, Q. Tao, Z.-A. Xu, and G.-H. Cao, *A new ferromagnetic superconductor: $CsEuFe_4As_4$*, Sci. Bull. 61 (2016), pp. 1213–1220

[5] W.R. Meier, T. Kong, U.S. Kaluarachchi, V. Taufor, N.H. Jo, G. Drachuck, A.E. Böhmer, S.M. Saunders, A. Sapkota, A. Kreyssig, M.A. Tanatar, R. Prozorov, A.I. Goldman, F.F. Balakirev, A. Gurevich, S.L. Bud'ko, and P.C. Canfield, *Anisotropic thermodynamic and transport properties of single-crystalline $CaKFe_4As_4$*, Phys. Rev. B 94 (2016), p. 064501.

[6] L.N. Bulaevskii, A.I. Buzdin, M.L. Kulić, and S.V. Panjukov, *Coexistence of superconductivity and magnetism theoretical predictions and experimental results*, Adv. Phys. 34 (1985), pp. 175–261.

[7] S. Zapf and M. Dressel, *Europium-based iron pnictides: A unique laboratory for magnetism, superconductivity and structural effects*, Rep. Prog. Phys. 80 (2017), p. 016501.

[8] Y. Liu, Y.-B. Liu, Q. Tao, C.-M. Feng, and G.-H. Cao, *$RbEu(Fe_{1-x}Ni_x)_4As_4$: From a ferromagnetic superconductor to a superconducting ferromagnet*, Phys. Rev. B 96 (2017), p. 224510.

[9] J.-K. Bao, K. Willa, M.P. Smylie, H. Chen, U. Welp, D.Y. Chung, and M.G. Kanatzidis, *Single crystal growth and study of the ferromagnetic superconductor $RbEuFe_4As_4$*, Cryst. Growth Des. 18 (2018), pp. 3517–3523.
[10] M.P. Smylie, K. Willa, J.-K. Bao, K. Ryan, Z. Islam, H. Claus, Y. Simsek, Z. Diao, A. Rydh, A.E. Koshelev, W.-K. Kwok, D.Y. Chung, M.G. Kanatzidis, and U. Welp, *Anisotropic superconductivity and magnetism in single-crystal $RbEuFe_4As_4$*, Phys. Rev. B 98 (2018), p. 104503.
[11] M.A. Albedah, F. Nejadsattari, Z.M. Stadnik, Y. Liu, and G.-H. Cao, *Mössbauer spectroscopy measurements on the 35.5 K superconductor $Rb_{1-\delta}EuFe_4As_4$*, Phys. Rev. 97 (2018), p. 144426.
[12] C. Xu, Q. Chen, and C. Cao, *Unique crystal field splitting and multiband RKKY interactions in Ni-doped $EuRbFe_4As_4$*, Commun. Phys. 2 (2019), p. 16.
[13] P. Blaha, K. Schwartz, G. Madsen, D. Kvasnicka, and J. Luitz, *WIEN2k: An Augmented Plane Wave Plus Local Orbitals Program for Calculating Crystal Properties*, Karlheinz Schwarz, Technical Universität Wien, Austria, 1999.
[14] F. Nejadsattari, P. Wang, Z.M. Stadnik, Y. Nagata, and T. Ohnishi, *Ab-initio, magnetic, and ^{155}Gd Mössbauer spectroscopy study of $GdRhO_3$*, J. Alloys Compd. 725 (2017), pp. 1098–1105.
[15] J.P. Perdew, S. Burke, and M. Ernzerhof, *Generalized gradient approximation made simple*, Phys. Rev. Lett. 77 (1996), pp. 3865–3868.
[16] V.I. Anisimov and O. Gunnarsson, *Density-functional calculation of effective Coulomb interactions in metals*, Phys. Rev. B 43 (1991), p. 7570–7574.
[17] V.I. Anisimov, J. Zaanen, and O.K. Andersen, *Band theory and Mott insulators: Hubbard U instead of Stoner I*, Phys. Rev. B 44 (1991), p. 943–954.
[18] V.N. Antonov, B.N. Harmon, and A.N. Yaresko, *Electronic structure of mixed-valent and charge-ordered Sm and Eu pnictides and chalcogenides*, Phys. Rev. B 72 (2005), p. 085119.
[19] R.F.W. Bader, *Atoms in Molecules: A Quantum Theory*, Oxford University Press, Oxford, 1991.
[20] P.E. Blöchl, O. Jepsen, and O.K. Andersen, *Improved tetrahedron method for Brillouin-zone integrations*, Phys. Rev. B 49 (1994), pp. 16223–16233.
[21] A.P. Drozdov, P.P. Kong, V.S. Minkov, S.P. Besedin, M.A. Kuzovnikov, S. Mozaffari, J. Balicas, F.F. Balakirev, D.E. Graf, V.B. Prakapenka, E. Greenberg, D.A. Knyazev, M. Tkacz, and M.I. Eremets, *Superconductivity at 250 K in lanthanum hydride under high pressures*, Nature 569 (2019), pp. 528–531.
[22] Y.I. Seo, W.J. Choi, S. Kimura, and Y.S. Kwon, *Evidence for a preformed Cooper pair model in the pseudogap spectra of a $Ca_{10}(Pt_4As_8)(Fe_2As_2)_5$ single crystal with a nodal superconducting gap*, Sci. Rep. 9 (2019), p. 3987.
[23] A. Foley, S. Verret, A.-M.S. Tremblay, and D Sénéchal, *Coexistence of superconductivity and antiferromagnetism in the Hubbard model for cuprates*, Phys. Rev. B 99 (2019), p. 184510.
[24] X. Shi and G. Wang, *Electronic structure and magnetism of the multiband new superconductor $CaRbFe_4As_4$*, J. Phys. Soc. Jpn. 85 (2016), p. 124714.
[25] F. Lochner, F. Ahn, T. Hickel, and I. Eremin, *Electronic properties, low-energy Hamiltonian, and superconducting instabilities in $CaKFe_4As_4$*, Phys. Rev. B 96 (2017), p. 094521.
[26] D.V. Suetin and I.R. Shein, *Electronic properties and Fermi surface for new layered high-temperature superconductors $CaAFe_4As_4$ (A = K, Rb, and Cs): FLAPW-GGA calculations*, J. Supercond. Nov. Magn. 31 (2018), pp. 1683–1692.

[27] M. Hashimoto, I.M. Vishik, R.-H. He, and T.P. Devereaux, *Energy gaps in high-transition-temperature cuprate superconductors*, Nature Phys. 10 (2014), pp. 483–495.
[28] A. Chubukov, *Chubukov, Iron-based super conductivity*, in *Springer Series in Materials Science*, P. D. Johnson, G. Xu, W.-G. Yin, eds., Berlin: Springer, 2015. pp. 255–329.
[29] F. Birch, *Finite elastic strain of cubic crystals*, Phys. Rev. 71 (1947), pp. 809–824.
[30] F.D. Murhanghan, *The compressibility of media under extreme pressures*, Proc. Natl. Acad. Sci. 30 (1944), pp. 244–247.
[31] N.N. Greenwood and T.C. Gibb, *Mössbauer Spectroscopy*, Chapman and Hall, London, 1971.
[32] P. Gütlich, E. Bill, and A. Trautwein, *Mössbauer Spectroscopy and Transition Metal Chemistry*, Springer, Berlin, 2011.
[33] P. Blaha, *Calculations of Mössbauer parameters in solids by DFT bandstructure calculations*, J. Phys.: Conf. Series 217 (2010), p. 012009.
[34] F. Nejadsattari, Z.M. Stadnik, and J. Żukrowski, *Mössbauer spectroscopy study of a new layered iron oxyselenide $Na_2Fe_2Se_2O$*, J. Alloys Compd. 639 (2015), pp. 547–555.
[35] U.D. Wdowik and K. Reubenbauer, *Calibration of the isomer shift for the 14.4-keV transition in ^{57}Fe using the full-potential linearized augmented plane-wave method*, Phys. Rev. B 76 (2007), p. 155118.
[36] F. Nejadsattari, Z.M. Stadnik, J. Przewoźnik, and K.H.J. Buschow, *Mössbauer spectroscopy, magnetic, and ab-initio study of the Heusler compound Fe_2NiGa*, Physica B 477 (2015), pp. 113–122.
[37] G. Martínez-Pinedo, P. Schwerdtfeger, E. Caurier, K. Langanke, W. Nazarewich, and T. Söhnel, *Nuclear quadrupole moment of ^{57}Fe from microscopic nuclear and atomic calculations*, Phys. Rev. Lett. 87 (2001), p. 062701.